

# Covalently-Bonded Laminar Assembly of Van der Waals Semiconductors with Polymers: Toward High-Performance Flexible Devices

Ningxin Li, Tara Jabegu, Rui He, Seokjoon Yun, Sujoy Ghosh, Diren Maraba, Olugbenga Olunloyo, Hedi Ma, Aisha Okmi, Kai Xiao, Gangli Wang, Pei Dong,\* and Sidong Lei\*

Van der Waals semiconductors (vdWS) offer superior mechanical and electrical properties and are promising for flexible microelectronics when combined with polymer substrates. However, the self-passivated vdWS surfaces and their weak adhesion to polymers tend to cause interfacial sliding and wrinkling, and thus, are still challenging the reliability of vdWS-based flexible devices. Here, an effective covalent vdWS-polymer lamination method with high stretch tolerance and excellent electronic performance is reported. Using molybdenum disulfide (MoS2) and polydimethylsiloxane (PDMS) as a case study, gold-chalcogen bonding and mercapto silane bridges are leveraged. The resulting composite structures exhibit more uniform and stronger interfacial adhesion. This enhanced coupling also enables the observation of a theoretically predicted tension-induced band structure transition in MoS<sub>2</sub>. Moreover, no obvious degradation in the devices' structural and electrical properties is identified after numerous mechanical cycle tests. This high-quality lamination enhances the reliability of vdWS-based flexible microelectronics, accelerating their practical applications in biomedical research and consumer electronics.

1. Introduction

Flexible microelectronics are receiving great attention to meet the increasing demand for wearable devices, [1-3] miniature health monitors, [4,5] and medical implantation. [6,7] These devices can also serve as human–machine interfaces in line with the

development of extended reality,[8] and the Internet of Things (IoT).[9] Among many semiconductor materials, van der Waals semiconductors (vdWS) are considered attractive candidates for flexible device fabrication, thanks to their excellent bendability,[10,11] ductility,[12] and outstanding electronic properties.[13,14] Due to their ultrathin thickness, vdWS devices are typically packaged with polymer-supporting substrates, such as polydimethylsiloxane (PDMS), to enhance their mechanical strength and facilitate general handling.[15,16] Nevertheless, the vdWS dangling bond-free surfaces lead to weak adhesion to polymer substrates.[17] Consequently, stretching, bending, and other mechanical deformations of the polymer supporting substrates cannot be coupled to the vdWS effectively, resulting in interfacial slippage, device wrinkling, peeling, and eventually failure.[18-20] Several attempts have been made to enhance the adhesion,[20-23] and overcome the above

issues. For example, an early attempt employed micro metal clamps which can pin vdWS layer edges onto the substrate, [23] but they cannot avoid sliding or wrinkling in the center. After that, the polymer encapsulation method [20] claims that it can provide stronger interlayer adhesion compared with the

N. Li, T. Jabegu, D. Maraba, A. Okmi, S. Lei Department of Physics and Astronomy Georgia State University Atlanta, GA 30303, USA E-mail: slei@gsu.edu R. He, P. Dong

Department of Mechanical Engineering George Mason University

Fairfax, VA 22030, USA É-mail: pdong3@gmu.edu

Center for Nanophase Materials Sciences Oak Ridge National Laboratory Oak Ridge, TN 37831, USA O. Olunloyo Department of Physics and Astronomy University of Tennessee, Knoxville Knoxville, TN 37996, USA

H. Ma, G. Wang Department of Chemistry Georgia State University Atlanta, GA 30303, USA

S. Yun, S. Ghosh, K. Xiao

The ORCID identification number(s) for the author(s) of this article can be found under https://doi.org/10.1002/smll.202310175

DOI: 10.1002/smll.202310175

16136829, 0, Downloaded from https://onlinelibrary.wiley.com/doi/10.1002/smlt.202310175 by GEORGIA STATE UNIVERSITY, Wiley Online Library on [28/02/2024]. See the Terms and Conditions (https://onlinelibrary.wiley.com/kerm

conditions) on Wiley Online Library for rules of use; OA articles are governed by the applicable Creative Commons

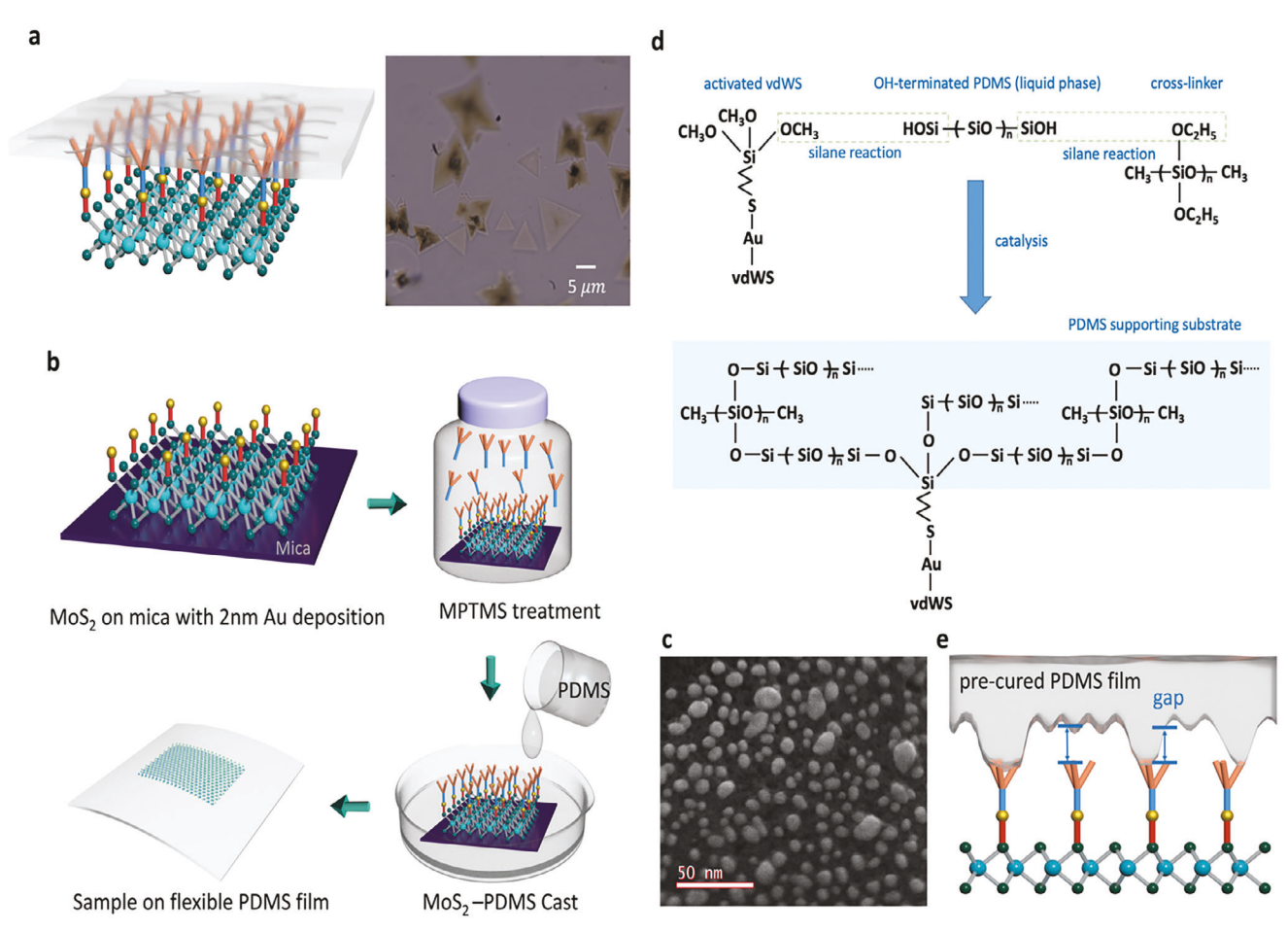


Figure 1. Principle and schematic of interfacial functionalization strategy. a) (Left) The interfacial lamination structure with coordinated chemical reaction for functionalization. The materials from bottom to top are molybdenum disulfide ( $MoS_{21}$ , Au, (3-mercaptopropyl)trimethoxy silane (MPTMS), and hydroxyl-terminated polydimethylsiloxane (PDMS), respectively. (Right) Optical microscope mage of monolayer MoS<sub>2</sub> on PDMS obtained by using the interfacial functionalization strategy. b) Workflow of the interfacial functionalization strategy. The MPTMS treatment bottle is filled with the MPTMS vapor whose molecules carry thiol group (-SH). c) Scanning transmission electron microscopy image of the deposited Au nanoparticles. d) Reaction scheme of salination between the hydroxyl groups in PDMS and the MPTMS molecules (multiple cross-linked structures may be formed). e) Demonstration of poorer contacts if directly laminate the MPTMS-functionalized vdWS to a pre-cured PDMS substrate.

conventional metal clamps, but it did not accurately explain the source and formation mechanism of the adhesion, which makes this conclusion and results still questionable. Moreover, these solutions rarely deliver uniform lamination between vdWS and polymer substrates. The uneven deformation and local strain accumulation in such structures may tear the vdWS layers, hindering the devices' endurance and robustness. Therefore, lamination between vdWS and polymer substrates still challenges the fabrication and application of vdWS-based flexible and stretchable devices.

To surmount this obstacle, we report a versatile strategy for vdWS-polymer lamination with outstanding mechanical strength, scalability, uniformity, and more importantly, optoelectronic performance. The fundamental principle of our method is to activate the vdWS surfaces through a gold-chalcogen reaction, from where thiol-terminated silane molecules can bridge the gold-activated vdWS to polymer substrate via salinization reaction. The resulting structure exhibits excellent interfacial quality, mechanical stability, and robustness, as well as outstanding optoelectronic performance. In addition to advancing the practical applications of vdWS flexible devices in medical treatment,[24,25] motion control, [26,27] biosensors, [28,29] and other critical fields, the as-fabricated vdWS-polymer composite structures can also serve as platforms to investigate phase transition, electronic structure evolution, and other intriguing fundamental materials processes under mechanical stimuli.

#### 2. Discussion

Transition metal dichalcogenides (TMDCs) and other widely studied vdWS typically have cleavage surfaces intrinsically passivated with chalcogen anions. These anions can usually bond with gold, silver, and other metal atoms strongly through coordinated chemical reactions.[30-32] Inspired by this mechanism, we design a vdWS-polymer interfacial laminar structure, as illustrated in Figure 1a. First, from bottom to top, vdWS surfaces are decorated with gold atoms, which are then covalently bonded to (3-mercaptopropyl) trimethoxy silane (MPTMS) molecules

www.small-journal.com

16136829, 0, Downloaded from https://onlinelibrary.wiley.com/doi/10.1002/smlt.202310175 by GEORGIA STATE UNIVERSITY, Wiley Online Library on [2802/2024]. See the Terms and Conditions (https://onlinelibrary.wiley.com/rems-ad-conditions) on Wiley Online Library for rules of use; OA aricles are governed by the applicable Creative Commons Licensed

through the gold-thiolate chemistry.<sup>[33]</sup> The trimethoxy silane (-Si-OCH<sub>3</sub>) groups on the other end of the MPTMS molecules then react with hydroxyl (-OH) on the polymer substrates, firmly anchoring the gold-activated vdWS.

To experimentally implement this above design, we establish a process workflow, as shown in Figure 1b. We employ molybdenum disulfide (MoS<sub>2</sub>) and PDMS as examples of vdWS and polymer substrates, respectively, to investigate the process without losing versatility. First, multilayer MoS2 obtained through mechanical exfoliation or monolayer MoS2 prepared via chemical vapor deposition (CVD) are transferred temporarily on mica or poly-(bisphsurfaceenol A carbonate) (PBAC) substrates. 1-2 nm of gold is then thermally deposited on these samples. Instead of forming continuously conductive layers, such a thin deposition creates discrete gold nanoparticles bonded to the 2D surface without altering the electronic properties significantly, as indicated by the subsequential optoelectronic measurements discussed in the following content. Figure 1c shows the scanning transmission electron microscopy (STEM) image that clearly reveals the distribution of deposited Au nanoparticles on the sample surface. Figure S1 (Supporting Information) exhibits another STEM image with lower magnification to demonstrate the large-scale uniform distribution of the particles. Further, atomic force microscopic (AFM) morphology and phase mappings also indicate the formation of nanoparticles, as shown in Figure S2 (Supporting Information). The reaction between MoS<sub>2</sub> and gold takes place spontaneously, as suggested by earlier investigations.[33,34] Our Raman scattering measurements also indicate the formation of Au-S bonds, manifested as the shifting of both E12 g (in-plane mode) and A<sub>10</sub> (out-of-plane mode) Raman peaks of MoS<sub>2</sub>, as observed in Figure S3 (Supporting Information).

Although the deposited Au particles do not form a continuous film, they may still alter the original electronic and optoelectronic properties of the MoS2 and affect the flexible device performance. Therefore, we employed photoconductivity measurement as shown in Figure S4 (Supporting Information). We find that the gold decoration enhances the photoresponse level by one order of magnitude. One possible explanation could be the plasmonic enhancement[35,36]

The gold-decorated MoS2 is then sealed in a container filled with MPTMS vapor for 3 h to form a fully covered self-assembled molecular monolayer. Subsequently, we cast the functionalized MoS<sub>2</sub> samples with a mixture of PDMS precursors. The mixture consists of hydroxyl-terminated PDMS (uncross-linked molecular chains in liquid phase), ethylsilicate serving as cross-linker, and catalysis to accelerate the curing process. The hydroxyl groups existing in this precursor are critically important for the successful lamination between MoS2 and PDMS, because they react with MPTMS and form anchor points, as illustrated in Figure 1d. (Refer to the Methods section for details.) It takes  $\approx$ 24 h for the PDMS mixture to cure at room temperature. After that, we can readily remove the laminated MoS<sub>2</sub> layers from the temporary mica or PBAC substrates and obtain samples with high quality and integrity, as exhibited in Figure 1a right panel.

To confirm the functions of gold and MPTMS in this lamination process, we also perform a control experiment with the same casting process but without gold decoration or MPTMS treatment. Obviously, MoS2 flakes cannot be effectively picked up from the mica temporary substrates even though the casted

PDMS form conformal geometry to the flakes, as shown in Figure S5 (Supporting Information). Therefore, the control experiment indicates the effectiveness of our interfacial functionalization for vdWS-polymer lamination.

It is essential to note that other widely used A-B two-part PDMS kits may not function properly for this workflow, due to the lack of hydroxyl groups. Further, we also find that it is difficult to laminate the MPTMS-functionalized vdWS layers directly to pre-cured PDMS substrates, even if oxygen plasma treatment is applied to create hydroxyl functional groups on the surfaces. This is because pre-cured PDMS is unlikely to have atomically flat geometry conformally matching vdWS surfaces, as shown in Figure 1e. The roughness or variations in the distances, even on a nanometer scale, are still too large compared with the Angstromsize MPTMS molecules to bridge the two parts. In other words, the anchor points are inadequate for a firm lamination. The corresponding optical image of MoS2 flakes that are poorly laminated on the pre-cured PDMS substrate can be found in Figure S6 (Supporting Information). In contrast, our functionalizing-andcasting procedure overcomes these issues and delivers a highquality vdWS-polymer composited structure for flexible device fabrication, as exhibited in Figure 1a right panel.

#### 3. Mechanical Characterization

For lamination quality examination, we carried out a tensile test and employed Raman spectroscopy to monitor the MoS2 deformation, as earlier studies did.[37,38] A home-built computercontrolled fixture was used to stretch PDMS substrates, as shown in Figure S7 (Supporting Information). Two sides of the PDMS substrates were clamped on the fixture, and their strains were automatically controlled by a step motor with 0.025% accuracy. As the PDMS film was being stretched, in situ Raman spectra were captured to identify the MoS<sub>2</sub> deformation.

Independent of the MoS2 flake thicknesses, all samples laminated with Au and MPTMS treatment exhibit obvious E1<sub>2,9</sub> peak shifting as strains build on the PDMS substrates, as demonstrated in Figure 2a,d, which is consistent with our expectations. (Raw Raman data is shown in Figure S8a,b, Supporting Information) The Raman peak shifting trend is also consistent with the earlier reports.<sup>[23,39,40]</sup> It is important to note that both Audecoration and strain can induce Raman peak shifting but with distinct features. As discussed above, the formation of Au-S bonds shifts both  $A_{1\sigma}$  and  $E^{1}_{2\sigma}$  peaks, because the chemical bonds change both out-of-plane and in-plane MoS2 lattice structures. In contrast, the tensile strain dominantly changes the inplane lattice structure, and thus, only affects the  $E^1_{\,2\,\mathrm{g}}$  mode. Meanwhile, the Au effect is permanent and constant, but the strain effect varies as a function of PDMS substrate deformation. Considering these factors, the chemical reaction-induced Raman shifting and mechanical deformation-induced one do not interfere with each other.

To better illustrate the peak shifting trend, we plot the peak positions as functions of strain and show them in Figure 2b,e. By comparing them, we find that under the same PDMS strain, thinner MoS<sub>2</sub> samples experience larger Raman peak shifting, showing an inversely proportional relationship, as illustrated in Figure S9 (Supporting Information). For layered material, MoS<sub>2</sub>, this relationship reveals that despite applying Au decoration

16136829, 0, Downloaded from https://onlinelibrary.wiley.com/doi/10.1002/smll.202310175 by GEORGIA STATE UNIVERSITY, Wiley Online Library on [28/02/2024]. See the Terms and Conditions (https://onlinelibrary.wiley.com/kerm

conditions) on Wiley Online Library for rules of use; OA articles are governed by the applicable Creative Commons License

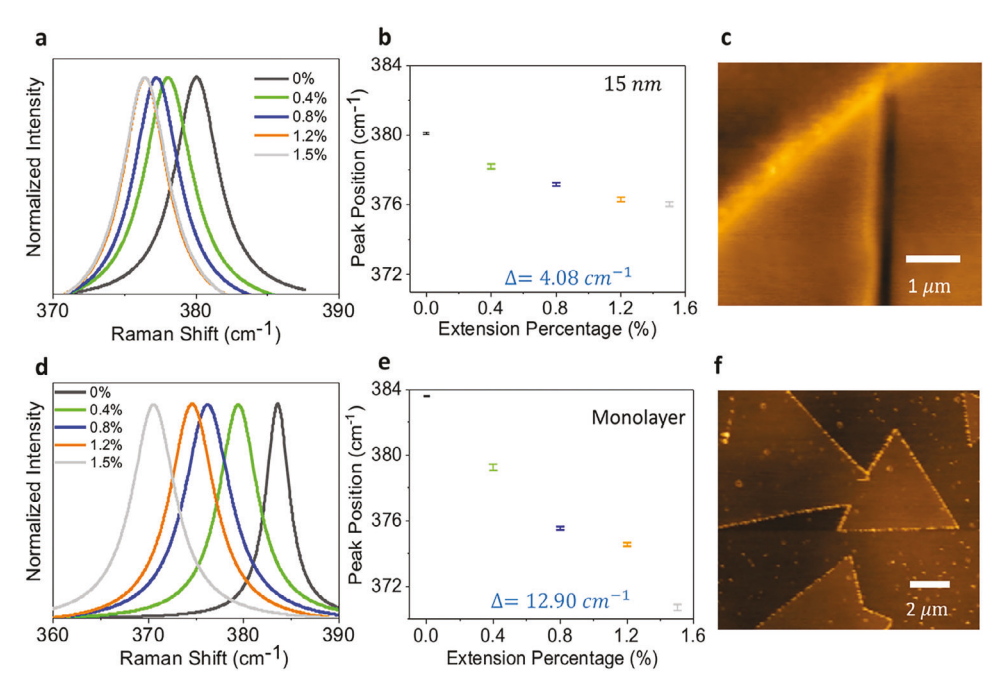


Figure 2. Lamination quality characterization for different MoS<sub>2</sub>-PDMS samples. a) Raman spectrum of 15 nm examined MoS<sub>2</sub> samples under different tensile strains. A subtle redshift phenomenon can be observed. b) The corresponding peak positions which were obtained from (a) under different tensile strains (error bar included). The Raman peak shifting magnitude is 4.08 cm<sup>-1</sup> from 0% to 1.5% strain. c) Atomic force microscopy (AFM) mapping of the 15 nm examined MoS<sub>2</sub> sample in (a) after stretching. d) Raman spectrum of monolayer examined CVD-MoS<sub>2</sub> sample under different tensile strains. An obvious redshift phenomenon can be observed. e) The corresponding peak positions obtained from (d) under different tensile strains (error bar included). The Raman peak shifting magnitude is 12.90 cm<sup>-1</sup> from 0% to 1.5% strain. f) AFM mapping of the examined CVD-MoS<sub>2</sub> sample in (d) after stretching.

exclusively to the surface of MoS2, mechanical deformation can propagate throughout the entire multilayer MoS2. This phenomenon occurs because, although MoS2 layers primarily exhibit van der Waals interactions, they share a common lattice structure and typically adopt a closely packed 2H order. Consequently, even if a unit cell has a relatively small interaction energy, [41] the interlayer adhesion can still be substantial due to the well-ordered packing between MoS2 layers.

This is because the same strain built similar stress in PDMS, whereas thicker MoS2 flakes have higher Young's modulus, [42] and thus, less deformation and Raman shifting. Through the entire test process, we do not observe any wrinkling or peeling (i.e., interfacial separation) after the stretching test in either the mechanically exfoliated thick samples or CVD monolayer samples, as evidenced by the AFM characterization shown in Figure 2c,f. All this experimental evidence indicates a high interfacial lamination quality that can effectively couple the PDMS deformation to the vdWS layer and ensure the composition structure integrity.

More importantly, we observe that monolayer MoS<sub>2</sub> (Figure 2e) follows the PDMS deformation up to a 1.50% strain with a peak shifting of 12.9 cm<sup>-1</sup>, which is much higher than the  $\approx$ 4.6 cm<sup>-1</sup> achieved on metal clamp samples,[23] and the 11.1 cm-1 with the polymer encapsulation method. [20] All this experimental evidence confirms that our strategy produces a much better interfacial adhesion between vdWS and polymer substrates, ensuring the integrity and endurance of their composite structures during mechanical cycles. The optical images of all the above-examined samples can be found in Figure \$10 (Supporting Information).

It is worth mentioning that our samples can stand a strain larger than the abovementioned 1.50% limit. In the experiment, we found samples can stand up to a 1.70% tensile strain, after which the E<sup>1</sup><sub>2,g</sub> peak starts to shift irregularly, suggesting that the interfacial separation takes place. For the specific experimental results, refer to Figure S11 (Supporting Information).

To better demonstrate the important role of interfacial functionalization in delivering reliable lamination between vdWS and flexible substrates. We perform control experiments on the stretching fixture but with MoS2-PDMS samples without any interfacial functionalization. The poor interface is illustrated in Figure 3a that only a few anchoring points exist, resulting in ineffective interlayer bonding. The control group shows no obvious peak shifting when the PDMS substrate is stretched, as shown in Figure 3b,c. (Smoothed Raman data is shown here. Refer to Figure S8c for raw data, Supporting Information) This is because the substrate deformation is not effectively coupled to the MoS<sub>2</sub> flakes due to weak interfacial adhesion, and the MoS2 flakes slide on the substrates without experiencing any deformation, as illustrated in Figure 3a. Even worse, after the strain is released, the recoiling of PDMS substrates creates wrinkles in the vdWS layers, as indicated by the atomic force microscopic (AFM) measurement shown in Figure 3d. Figure 3a also illustrates the wrinkle forming process.

Other than Raman spectroscopy, a photoluminescence (PL) study can also be used to monitor the band structure change of the examined samples.<sup>[43,44]</sup> Thus, we also capture strain-dependent PL spectra and plot them in Figure S12

16136829, 0, Downloaded from https://onlinelibrary.wiley.com/doi/10.1002/smll.202310175 by GEORGIA STATE UNIVERSITY, Wiley Online Library on [28/02/2024]. See the Terms and Conditions (https://onlinelibrary.

ions) on Wiley Online Library for rules of use; OA articles are governed by the applicable Creative Commons

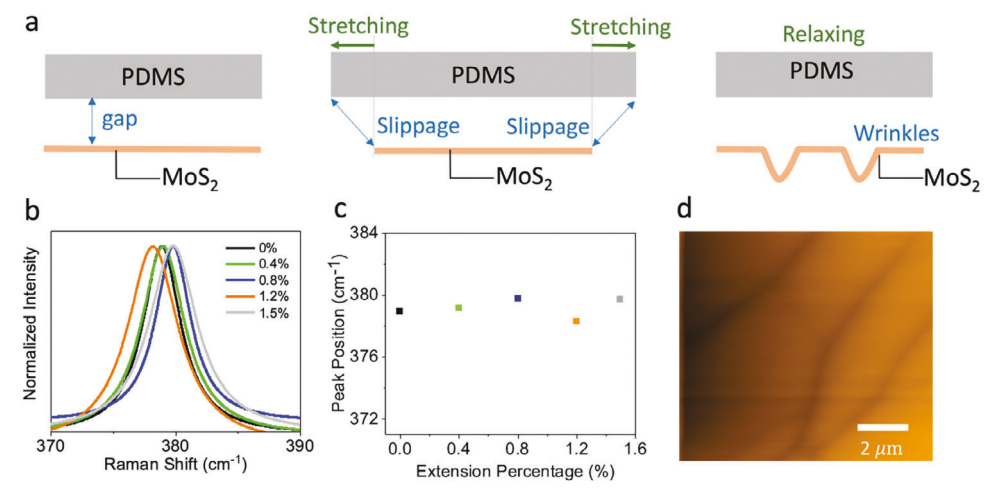


Figure 3. Schematically illustration of the mechanically stretching characterizations for untreated samples (control group). a) Demonstration of poorer contacts if directly laminates the unfunctionalized vdWS to a pre-cured PDMS substrate. b) Raman spectrum of the control group's sample under different tensile strains. c) The corresponding peak positions, which were obtained from (b) under different tensile strains. Under the action of continuously increasing tensile percentage, the irregular Raman shifting appears because of the existence of the interlayer slipper caused by weak bonding. d) AFM mapping of the control group's sample after stretching.

(Supporting Information). Similar to the Raman characterization, the PL peaks experience red shifting as the strain increases, a tensile strain can significantly decrease its bandgap, evidenced by the shifts from 1.87 to 1.66 eV, corresponding to a  $\Delta Eg$  (change in bandgap) of ≈210 meV. This value is larger than the previously achieved ones in monolayer MoS2 (ranging from 90-193 meV).[23,45,46]

All the above characterizations in terms of Raman, PL, and AFM studies indicate that our surface functionalization strategy delivers a better and more reliable lamination between vdWS and flexible substrates. The electronic and optoelectronic characterization shows that functionalization also improves the material properties. Based on these observations, we can fabricate flexible devices and investigate their performances, including mechanical effects, device robustness, and so forth.

#### 4. Flexible Device Fabrication and Characterization

The interfacial chemical bonding principle validated by the above experiments is not limited to the lamination between vdWS and polymers; instead, it can address another challenge for flexible device fabrication. Because of their softness, polymer substrates usually experience deformation during the regular spin coating, lithography, and other processes designed for rigid semiconductors. The deformation usually damages the manufacturing precision and scalability.[47,48] In contrast, our interfacial functionalization methods provide an alternative pathway to address this issue. As illustrated in Figure 4, we prepare devices on the rigid substrate in a conventional way, and then relocate and laminate the pre-fabricated devices onto flexible substrates (PDMS) with the above-introduced functionalization procedure. It is essential to underscore that the success of this workflow hinges on the surface functionalization. Strong interlayer adhesion plays a pivotal role in ensuring the reliability of relocation, thereby preventing any unnecessary interlayer sliding. Moreover, the strategy can drastically improve fabrication precision and scalability. Meanwhile, the produced high-quality devices allow us to insightfully investigate the electronic property evolution of vdWS under mechanical deformation.

Specifically, the flexible device fabrication workflow includes steps of regular device fabrication on rigid substrates, followed by relocation, and lamination. Mechanically exfoliated or CVD vdWS are first transferred onto flat rigid substrates, such as Si/SiO<sub>2</sub>, coated with poly(methylmethacrylate) (PMMA). The PMMA coating serves as a sacrificial layer for the flexible device separation as introduced later. Then, a regular photolithography process with S1805 photoresist and undercut layer polydimethylglutarimide(PMGI) is employed to generate electrode patterns, followed by development with a tetramethylammonium hydroxide (TMAH)-based developer, which does not dissolve the PMMA. After that, we expose the developed photoresist pattern with ultraviolet (UV) light for a second time before the metal deposition. Gold serves as the contact electrode for two reasons. 1) It tends to form good contact with MoS2 and many other vdWS.[49] 2) It can be directly functionalized with MPTMS and other mercapto-linker-silanes, and then bridged to PDMS with the same reaction mechanism, as shown in Figure 1a. Subsequential to the metal deposition, the same alkaline-based developer is used to remove double-exposed \$1805 photoresist for metal deposition lift-off. These regular semiconductor process steps render functional devices on the flat rigid substrate with high precision and scalability. Here, the usage of acetone and other organic should be avoided for the lift-off step to preserve the PMMA coating. Subsequentially, a 1-2 nm layer of gold is deposited to decorate the vdWS with nanoparticles, followed by MPTMS functionalization and PDMS casting, as introduced above and illustrated in Figure 1b. Here, it is essential to emphasize that, similar to the standard lithography techniques, the gold utilized as electrodes will create a continuous film to fulfill their conductive functions. In contrast, the 1-2 nm deposition of gold carried out after the lift-off process, will have the formation of discrete nanoparticles. These individual nanoparticles

www.small-journal.com

16136829, 0, Downloaded from https://onlinelibrary.wiley.com/doi/10.1002/smll.202310175 by GEORGIA STATE UNIVERSITY, Wiley Online Library on [28/02/2024]. See the Terms and Conditions (https://onlinelibrary.wiley.

nditions) on Wiley Online Library for rules of use; OA articles are governed by the applicable Creative Commons

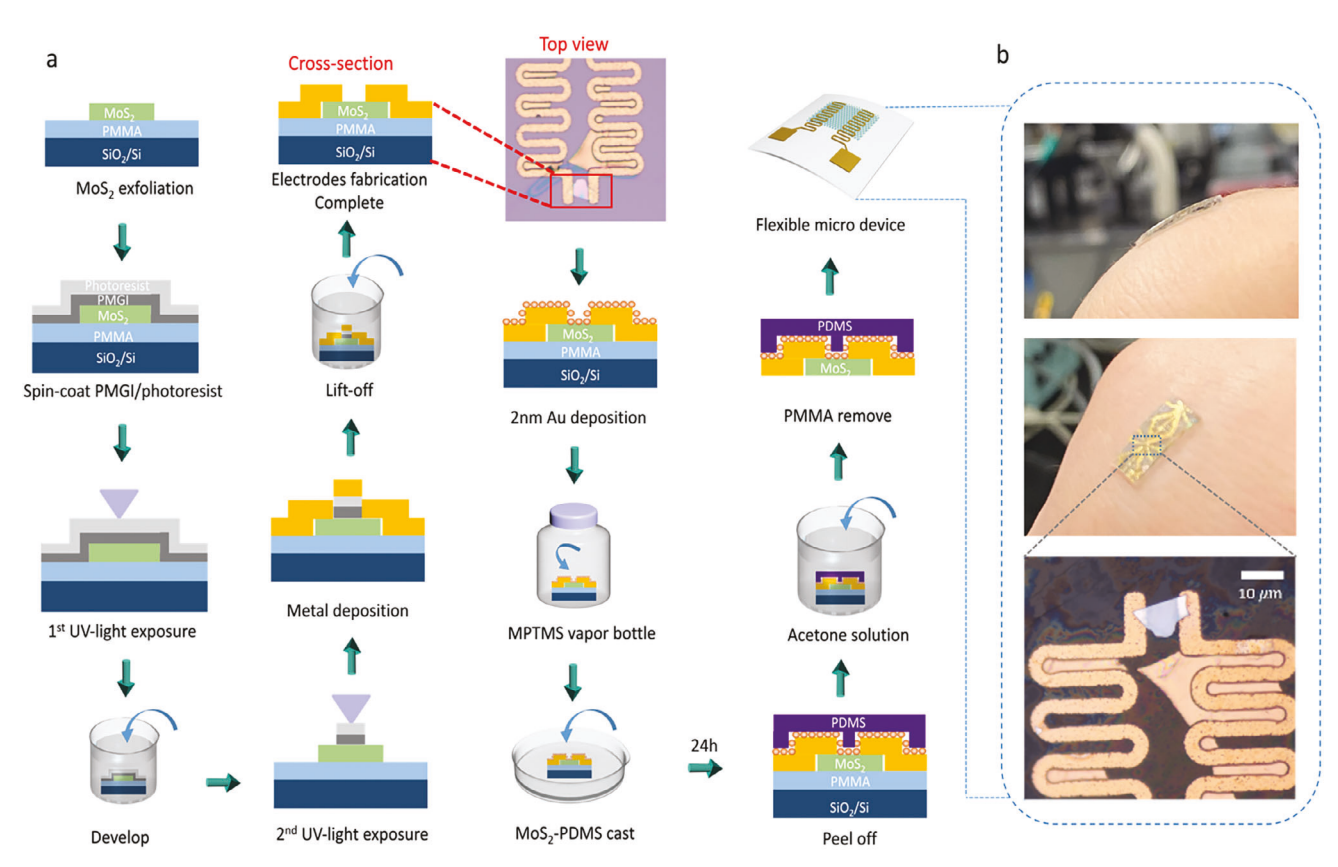


Figure 4. Interfacial functionalization-based flexible device fabrication technology and device-skin fit adaptability display. a) Cross-section view of workflow for device fabrication, relocation, and lamination process. b) Side and front views with a zoom-in view of the adaptability of the flexible device obtained from interfacial functionalization strategy to human skin while bending force is applied.

solely serve the purpose of creating Au—S bonds, as illustrated in Figure 1d, without contributing to the overall conductivity. The detailed functions' difference between these two Au is shown in Figure \$13 (Supporting Information).

After the PDMS cures, acetone is used to dissolve the PMMA coating and release the flexible devices, as demonstrated in Figure 4a (Refer to Experimental Section for more information). The devices obtained through this procedure show excellent mechanical flexibility and fit well with human skin under various moving conditions, as shown in Figure 4b. Therefore, our method fully exploits the intrinsic flexibility and stretchability of vdWS devices for medical treatment, [24,25] motion control, [26,27] biosensors, [28,29] and other critical applications.

Once the flexible device was successfully constructed, we performed a series of optoelectronic characterizations to verify the device's performance, particularly under the effects of interfacial lamination and mechanical deformation. Photoresponse spectra directly measure the energy band structure of vdWS, as such, can unveil many details about the lamination and deformation impacts. Figure 5a shows the photoresponse spectra of the device under different strain values. Under low strain, the device always has a strong photoresponse to blue light. Besides, a peak located at 650 nm corresponds to the intraband excitation. These observations agree with previously reported MoS<sub>2</sub> photoresponse spectra, [50] indicating that the laminated MoS2 is still semiconductor in characteristics, despite the thin gold deposition. They also, in turn, prove that the 1-2 nm gold deposition provides sufficient discrete isolated anchor points rather than a continuous conductive film for MPTMS functionalization.

The photoresponse spectra do not vary dramatically as the strain increases, suggesting that MoS2 maintains to be semiconductor under strain up to 1.5%. A closer inspection also reveals a slight red shifting as the strain increases (Figure 5a inset), and this phenomenon matches the observations in Photoluminescence (PL) measurements. When the strain exceeds 0.6%, the 650 nm response peak sustains disappears. This agrees with an earlier theoretical simulation predicting a strain-induced direct band-to-indirect band phase change in MoS<sub>2</sub> [51] The perfect match between the theoretical and experimental results, in turn, suggests that the PDMS strain is efficiently coupled to the MoS<sub>2</sub> devices, thanks to the covalent bonding on their interfaces.

Besides the spectral study, we also performed photoconductivity (I–V) measurements, as exhibited in Figure 5b. Frist, the MoS<sub>2</sub> device was excited with red (647 nm), green (568 nm), and blue (488 nm) laser sources successively with no tensile strain applied. The device shows distinct responses to all three excitations, with the bias voltage within  $\pm$  0.1 V. The linearity of all I–V curves indicates good Ohmic-like contact between MoS2 and gold electrodes, as suggested by earlier investigations.<sup>[52,53]</sup> Meanwhile, the dark current (Figure 5b inset) of the device is extremely low, approaching the noise level of the experimental setup employed for this measurement. This low dark current, again, proves that the

16136829, 0, Downloaded from https://onlinelibrary.wiley.com/doi/10.1002/smll.202310175 by GEORGIA STATE UNIVERSITY, Wiley Online Library on [28/02/2024]. See the Terms and Conditions (https://onlinelibrary.

tions) on Wiley Online Library for rules of use; OA articles are governed by the applicable Creative Commons License

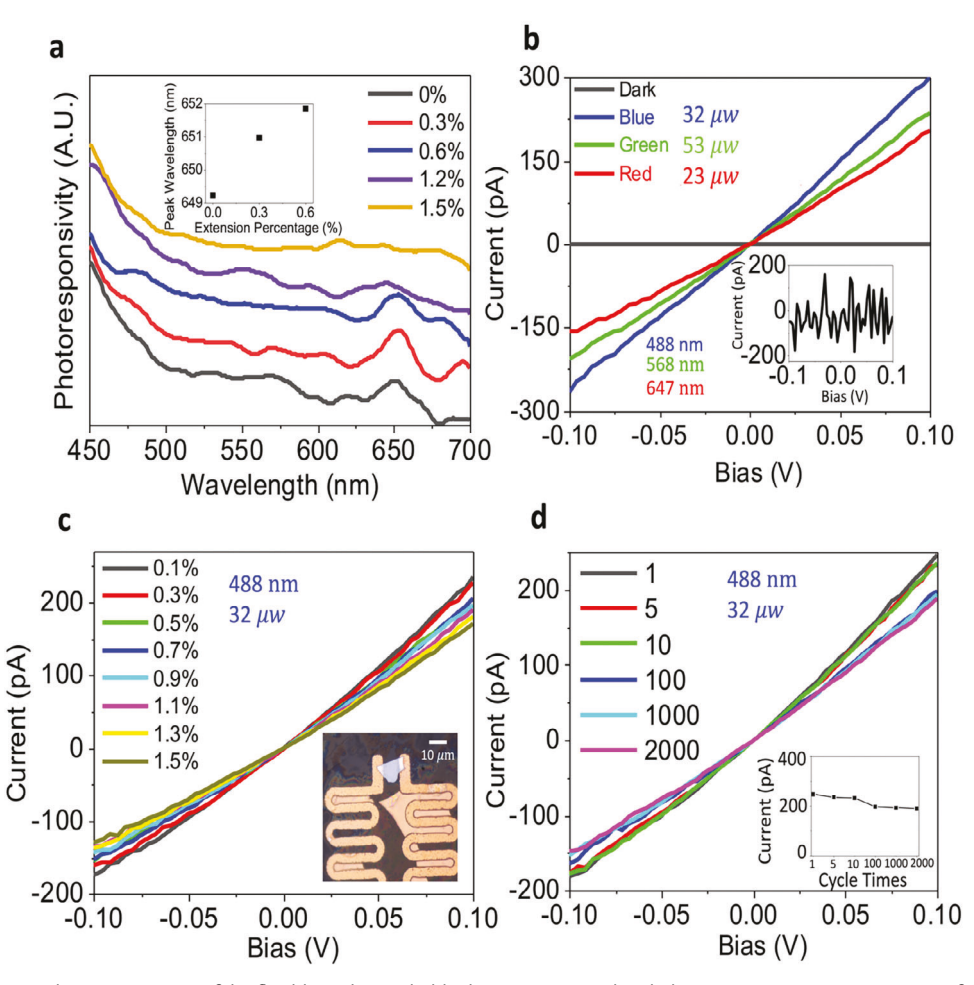


Figure 5. Optoelectronic characterizations of the flexible and stretchable device. a) Normalized photoresponsivity (P.R.) spectra of the relocated flexible device with a bias voltage of 0.1 V. (inset) Slightly red-shift trend of the 650 nm peak until the tensile reaches 0.6%. Gaussian fitting function is applied to obtain peak positions. b) Photocurrent curves of the relocated flexible device excited by red (647 nm), green (568 nm), and blue (488 nm) laser light sources with a bias voltage of ±0.1 V. This measurement was finished without tensile strains. (inset) A dark current curve is shown. c) Photocurrent curves of the relocated flexible device under different tensile strains with a bias voltage of 0.1 V. The photocurrent value fluctuates slightly during the stretching process. The excitation laser wavelength is 488 nm. (inset) Optical image of the relocated flexible and stretchable device. d) Photocurrent curves of the relocated flexible device under multiple cyclic stretching tests while the strain is up to 1.5%. The photocurrent values attenuated slightly during the multiple stretching-relaxing processes. The excitation laser wavelength is 488 nm. (inset) Current-cycle times (I-t) relationship under bias 0.1 V.

1-2 nm gold deposition and MPTMS functionalization do not form any conductive channels that hinder device performances.

Figure 5c shows the photocurrent response as a function of tensile strain. Figure 5c inset shows the optical microscope image of the examined device. A 488 nm excitation was used for this investigation. It is found that the I-V curves gradually decrease as the strain increase but sustain the same order of magnitude with less than 20% in variation. After the strain is released, the current recovers to the original level, suggesting that the reduced photoresponse level is a strain-effect instead of device damage. To better verify the device's robustness, we perform a mechanical cycling test by measuring the photocurrent levels after 1, 5, 10, 100, 1000, and 2000 cycles of tensile strain up to 1.5%, as shown in Figure 5d. and inset. No significant degradation in photocurrents is observed in these mechanical cycling tests, and the photocurrent recovers to the original level after the strain is removed.

Similar tests under other excitation wavelengths show the same results, as shown in Figure \$14 (Supporting Information).

In addition to the abovementioned changes in mechanical and electrical properties, other effects, such as piezoelectricity, [54] can be potentially generated along with the device deformation. Thus, our flexibility devices may also serve as power sources in wearable electronics.

These optoelectronic characterizations validate the following perspectives. 1) The gold decoration, MPTMS functionalization, and PDMS lamination cause no negative effects on MoS2 optoelectronic properties in terms of energy band structure, photoresponsivity, and dark current level. 2) The interfacial lamination provides outstanding mechanical endurance and robustness that stand tremendous stretching cycles, without showing significant performance decay or structural variation. 3) Thanks to the effective mechanical coupling between vdWS and polymer

5. Conclusion

www.advancedsciencenews.com

substrates, we are able to effectively create mechanical defor-

mations on vdWS and study their response to extreme condi-

tions that are intangible in previous device structures. All these

benefits open up new pathways toward vdWS-based flexible and

stretchable device fabrication and application. Meanwhile, as-

constructed devices can serve as promised platforms to inves-

tigate the fundamental mechanical and electronic properties of

In summary, we introduce a new principle and workflow for

vdWS flexible device fabrication, emphasizing uniform and

strong covalent lamination with polymer supporting substrates.

Compared with other methods, our strategy can better couple

the polymer deformation to the vdWS layers to ensure the re-

liability of the flexible/stretchable devices, and drastically elon-

gate their lifetime. As-constructed wearable sensors show ex-

cellent mechanical stability and electronic performance. No ob-

vious peeling, wrinkling, or electronic performance decay can

be detected after a few thousands mechanical stretching cycles.

The enhanced vdWS-polymer adhesion also drastically increases

the achievable vdWS deformation, and thus, enables the experi-

mental observation of a theoretically predicted direct-to-indirect

energy band transition. The introduced principle and workflow

versatilely apply to chalcogen-passivated vdWS and hydroxylated

polymer substrates, delivering effective lamination otherwise un-

achievable by other procedures. The drastically enhanced struc-

tural stability and electrical reliability will foster the development

and application of vdWS-based flexible/stretchable devices in bi-

ological sensors, medical devices, consumer electronics, human-

machine interfaces, and other emerging fields.

vdWS with improved accuracy and consistency.

fluid to part B was 10:1. After mixing these two parts according to the proportion, a desiccator was used to remove air bubbles in the mixture, and then the filler was slowly poured on the surface of the sample until it was completely covered. After curing, the PDMS film could be readily detached from the temporary substrates with the samples or devices attached to it.

Material Characterization: The optical image was captured with the Olympus BX60. The scanning transmission electron microscopy (STEM) imaging was performed by using an aberration-corrected STEM Hitachi HD2700 working at an acceleration voltage of 120 kV. The spatial resolution was ≈1.5 A. High-angle annular dark field (HAADF), bright field (BF) and secondary electron (SE) detectors were equipped in the HD2700. The AFM study was performed on the Veeco MultiMode V AFM system under tapping mode. Raman measurements were finished on a homebuilt confocal microscopy system with a 514 nm excitation. An Andor Shamrock 500i spectrometer and an Andor iDus 420 CCD camera were employed for Raman spectra capturing. This spectrometer captured the unique signature peaks of materials at specific wavenumbers when stimulated by a 532 nm laser, utilizing Raman scattering. The measurement system boasted impressive wavelength accuracy and repeatability, with values of 0.04 nm and 10 pm, respectively. Signal-to-noise levels were meticulously assessed, as depicted in Figure S15 (Supporting Information), confirming compliance with rigorous standards for quantitative analysis. The photoresponsivity spectra and IV curves were captured on a home-built probe station with the collaboration of a source meter unit (SMU, Keithley 2634B). A Bio-Rad argon-krypton ion laser was employed to generate the 488, 568, and 647 nm excitation for I-V tests. The photo-response spectra (P.R.) of the device shown in Figure 5a were calculated with the equation of  $R(\lambda) = [I_{light}(\lambda) - I_{dark}]/P(\lambda)$  under different stretching degrees, respectively. MoS2 field effect transistors (FET) werefabricated by using standard electron-beam lithography. The electrode patterns were then exposed with a 40 nA E-Beam current (Jeol-8100FS) followed by pattern development in MIBK/IPA (1:3) solution. Finally, Cr/Au (10nmn/50 nm) metal depositions were carried out by E-Beam evaporation at  $\approx 2 \times 10^{-6}$  Torr, and the remaining resist was removed in an acetone bath.

Device Fabrication and Relocation: For the device fabrications in this study, PMMA (Kem Lab 1000 harp eb 0.3) was first spin-coated on the silicon dioxide, after exfoliating MoS<sub>2</sub> on top of it, another two layers with 100 nm undercut resist (Kayaku Advanced Material PMGI SF 3S) and 300 nm S1805 photoresist (Kayaku Advanced Material S1805) were spin-coated on the sample. Then, a home-built 450 nm diode laser direct writing system was employed to expose electrodes for optoelectronic testing. After finishing the exposure, the patterns were obtained by soaking in the tetramethylammonium hydroxide (TMAH)-based developer (Kem Lab TMAH Developer 0.26N) for 30 s, followed by a second 60S ultraviolet light exposure. Next, the thermal evaporation (Au 45 nm) was done and metal lift-off procedures with tetramethylammonium hydroxide (TMAH)-based developer to complete the device fabrication. After finishing the lithography processes, the surface functionalization was applied by depositing another 1-2 nm Au and the 3 h MPTMS treatment. Next, the liquid PDMS was cast evenly on the surface of the device. After 24 h of curing, the PDMS film and the microdevice on it could be gently peeled off. Then the PMMA was removed by acetone, and the entire device manufacturing process was completed.

# 6. Experimental Section

Material Synthesis: The monolayer MoS<sub>2</sub> crystal was synthesized by CVD method with a 2-inch diameter hinged tube furnace (Lindberg/Blue). [55-57] Silicon wafers with 300 nm SiO<sub>2</sub> (Si/SiO<sub>2</sub>) were used as the growth substrate. The substrate was cleaned with acetone and isopropanol (IPA), and spin-coated with perylene-3,4,9,10-tetracarboxylic acid tetrapotassium salt, then it was dried. The Si/SiO2 wafers were later placed face-down above an alumina crucible containing 5 g of MoO<sub>3</sub> powder (99.9%, Sigma-Aldrich). Another crucible containing ≈ 0.7 g of S powder was placed 20 cm upstream from the center of the quartz tube. After evacuating the tube to  $\approx 5 \times 10^{-3}$  Torr, 70 sccm (standard cubic centimeter per minute) of argon and 6 sccm hydrogen gas were introduced into the tube. The temperature of the furnace was ramped up to 750 °C (with a ramping rate of 30 °C min  $^{-1}$  ) and maintained between 4-6 min at a pressure of 20 Torr. At 750 °C the location of the S powder was  $\approx$  180 °C. After growth, the furnace was allowed to cool naturally to room temperature. Bulk MoS<sub>2</sub> crystal for mechanical exfoliation was purchased from SPI Supplies.

Sample Preparation: The exfoliation of multilayer MoS<sub>2</sub> on the mica was done using blue tape (Nitto SPV224PR-MJ). The CVD MoS<sub>2</sub> was transferred on PBAC film instead of mica. The thin Au deposition (1–2 nm) was performed in an Edwards Auto 306 thermal evaporator. MPTMS (CAS# 4420-74-0) was purchased from Sigma–Aldrich. The PDMS precursors were purchased from Gelest Inc, and included two parts. Part A contained silanol-terminated polydimethylsiloxane (CAS#70131-67-8) and poly(dimethylsiloxane) (CAS#68412-37-3) while part B included silicone fluid and di-n-butyldilauryltin (CAS#77-58-7). The ratio between part A

# **Supporting Information**

Supporting Information is available from the Wiley Online Library or from the author

#### **Acknowledgements**

This work was supported by National Science Foundation DMR-2105126, ECCS-2238564, faculty start-up grant of Georgia State University, and Research Initiation Grant award of Georgia State University. G.W. and S.L. acknowledges the financial support from Georgia State University RISE award.  $\mbox{MoS}_2$  synthesis and processing was supported by the U.S.

16136829, 0, Downloaded from https://onlinelibrary.wiley.com/doi/10.1002/smll.202310175 by GEORGIA STATE UNIVERSITY, Wiley Online Library on [28/02/2024]. See the Terms and Conditions (https://onlinelibrary

on Wiley Online Library for rules of use; OA articles are governed by the applicable Creative Commons

Department of Energy, Office of Basic Energy Sciences, Division of Materials Sciences and Engineering. MoS<sub>2</sub> FET devices fabrication was conducted at the Center for Nanophase Materials Sciences, which is a DOE Office of Science User Facility. G. W. acknowledges the U.S. Department of Energy, Office of Science, Office of Basic Energy Sciences under Award Number DE-SC0019043. P. D. acknowledges the funding support by the Vehicle Technologies Office (VTO) in the Department of Energy (VTO CPS

#### **Conflict of Interest**

The authors declare no conflict of interest.

#### **Author Contributions**

N.L. and T.I. have contributed equally to this work, L.S. conceived and supervised the experimental and theoretical works. L.N., J.T., and L.S. designed and finished the interfacial functionalization tests for lamination. L.N., Y.S., G.S., and L.S. designed and fabricated the micro flexible device. O.O., O.A., and X.K. contributed to the synthesis and preparation of materials. L.N., M.D., and L.S. conceived, designed the optoelectrical characterization of devices and analyzed the data. L.N., J.T. and M.H. analyzed the experimental data and processed the images. L.N., H.R., W.G., D.P., and L.S. wrote the paper. All authors discussed the results and commented on the manuscript.

## **Data Availability Statement**

The data that support the findings of this study are available from the corresponding author upon reasonable request.

### Keywords

covalent lamination, flexible device, van der Waals semiconductors

Received: November 7, 2023 Revised: February 2, 2024 Published online:

- [1] W. Gao, H. Ota, D. Kiriya, K. Takei, A. Javey, Acc. Chem. Res. 2019, 52,
- [2] W. Gao, S. Emaminejad, H. Y. Y. Nyein, S. Challa, K. Chen, A. Peck, H. M. Fahad, H. Ota, H. Shiraki, D. Kiriya, Nature 2016, 529, 509.
- [3] S. Nakata, M. Shiomi, Y. Fujita, T. Arie, S. Akita, K. Takei, Nat. Electron.
- [4] M. Sang, K. Kang, Y. Zhang, H. Zhang, K. Kim, M. Cho, J. Shin, J. H. Hong, T. Kim, S. K. Lee, Adv. Mater. 2022, 34, 2105865.
- [5] X. Wang, Z. Liu, T. Zhang, Small 2017, 13, 1602790.
- [6] T. P. Huynh, H. Haick, Adv. Mater. 2018, 30, 1802337.
- [7] Y. Liu, M. Pharr, G. A. Salvatore, ACS Nano 2017, 11, 9614.
- [8] K. R. Pyun, J. A. Rogers, S. H. Ko, Nat. Rev. Mater. 2022, 7, 841.
- [9] L. Portilla, K. Loganathan, H. Faber, A. Eid, J. G. Hester, M. M. Tentzeris, M. Fattori, E. Cantatore, C. Jiang, A. Nathan, Nat. Electron. **2022**, 6, 10.
- [10] N. Li, A. Okmi, T. Jabegu, H. Zheng, K. Chen, A. Lomashvili, W. Williams, D. Maraba, I. Kravchenko, K. Xiao, ACS Nano 2022, 16,
- [11] R. F. Hossain, M. Min, L.-C. Ma, S. R. Sakri, A. B. Kaul, NPJ 2D Mater. Appl. 2021, 5, 34.

- [12] X. Wei, L. Mao, R. A. Soler-Crespo, J. T. Paci, J. Huang, S. T. Nguyen, H. D. Espinosa, Nat. Commun. 2015, 6, 8029.
- [13] F. Yang, S. Cheng, X. Zhang, X. Ren, R. Li, H. Dong, W. Hu, Adv. Mater. **2018**, *30*, 1702415.
- [14] Z. Gao, T.-R. Wei, T. Deng, P. Qiu, W. Xu, Y. Wang, L. Chen, X. Shi, Nat. Commun. 2022, 13, 7491.
- [15] S. B. Desai, G. Seol, J. S. Kang, H. Fang, C. Battaglia, R. Kapadia, J. W. Ager, J. Guo, A. Javey, Nano Lett. 2014, 14, 4592.
- [16] A. Castellanos-Gomez, R. Roldán, E. Cappelluti, M. Buscema, F. Guinea, H. S. van der Zant, G. A. Steele, Nano Lett. 2013, 13, 5361.
- [17] Y. Liu, Y. Huang, X. Duan, Nature 2019, 567, 323.
- [18] Z. Liu, M. Amani, S. Najmaei, Q. Xu, X. Zou, W. Zhou, T. Yu, C. Qiu, A. G. Birdwell, F. J. Crowne, Nat. Commun. 2014, 5, 5246.
- [19] E. M. Alexeev, N. Mullin, P. Ares, H. Nevison-Andrews, O. Skrypka, T. Godde, A. Kozikov, L. Hague, Y. Wang, K. S. Novoselov, ACS Nano 2020, 14, 11110.
- [20] Z. Li, Y. Lv, L. Ren, J. Li, L. Kong, Y. Zeng, Q. Tao, R. Wu, H. Ma, B. Zhao, Nat. Commun. 2020, 11, 1151.
- [21] L. Gong, I. A. Kinloch, R. J. Young, I. Riaz, R. Jalil, K. S. Novoselov, Adv. Mater. 2010, 22, 2694.
- [22] R. Frisenda, M. Drüppel, R. Schmidt, S. Michaelis de Vasconcellos, D. Perez de Lara, R. Bratschitsch, M. Rohlfing, A. Castellanos-Gomez, NPJ 2D Mater. Appl. 2017, 1, 10.
- [23] H. J. Conley, B. Wang, J. I. Ziegler, R. F. Haglund Jr, S. T. Pantelides, K. I. Bolotin, Nano Lett. 2013, 13, 3626.
- [24] M. Koleoso, X. Feng, Y. Xue, Q. Li, T. Munshi, X. Chen, Mater. Today Bio. 2020, 8, 100085.
- [25] C. Choi, M. K. Choi, S. Liu, M. S. Kim, O. K. Park, C. Im, J. Kim, X. Qin, G. J. Lee, K. W. Cho, Nat. Commun. 2017, 8, 1664.
- [26] V. K. Bandari, Y. Nan, D. Karnaushenko, Y. Hong, B. Sun, F. Striggow, D. D. Karnaushenko, C. Becker, M. Faghih, M. Medina-Sánchez, Nat. Electron. 2020, 3, 172.
- [27] T. Chen, Q. Shi, M. Zhu, T. He, L. Sun, L. Yang, C. Lee, ACS Nano **2018**, 12, 11561.
- [28] C. M. Boutry, L. Beker, Y. Kaizawa, C. Vassos, H. Tran, A. C. Hinckley, R. Pfattner, S. Niu, J. Li, J. Claverie, Nat. Biomed. Eng. 2019, 3, 47.
- [29] W. Liu, Y. Duo, J. Liu, F. Yuan, L. Li, L. Li, G. Wang, B. Chen, S. Wang, H. Yang, Nat. Commun. 2022, 13, 5030.
- [30] A. M. Chong, X. Zhao, A. T. Kustedjo, S. Qiao, Microporous Mesoporous Mater. 2004, 72, 33.
- [31] M. S. Inkpen, Z. F. Liu, H. Li, L. M. Campos, J. B. Neaton, L. Venkataraman, Nat. Chem. 2019, 11, 351.
- [32] Z. Liu, L. Ma, G. Shi, W. Zhou, Y. Gong, S. Lei, X. Yang, J. Zhang, J. Yu, K. P. Hackenberg, Nat. Nanotechnol. 2013, 8, 119.
- [33] H. Häkkinen, Nat. Chem. 2012, 4, 443.
- [34] J. Kim, S. Byun, A. J. Smith, J. Yu, J. Huang, J. Phys. Chem. Lett. 2013, 4, 1227.
- [35] X. Wang, S.-C. Huang, S. Hu, S. Yan, B. Ren, Nat. Rev. Phys. 2020, 2,
- [36] M. Rahaman, D. R. Zahn, J. Phys. Condens. Matter 2022, 34, 333001.
- C. Neumann, S. Reichardt, P. Venezuela, M. Drögeler, L. Banszerus, M. Schmitz, K. Watanabe, T. Taniguchi, F. Mauri, B. Beschoten, Nat. Commun. 2015, 6, 8429.
- [38] N. S. Mueller, S. Heeg, M. P. Alvarez, P. Kusch, S. Wasserroth, N. Clark, F. Schedin, J. Parthenios, K. Papagelis, C. Galiotis, 2D Mater. **2017**, 5, 015016.
- [39] H. Li, Q. Zhang, C. C. R. Yap, B. K. Tay, T. H. T. Edwin, A. Olivier, D. Baillargeat, Adv. Funct. Mater. 2012, 22, 1385.
- [40] C. Lee, H. Yan, L. E. Brus, T. F. Heinz, J. Hone, S. Ryu, ACS Nano 2010, 4. 2695.
- [41] W. L. Jorgensen, D. L. Severance, J. Am. Chem. Soc. 1990, 112, 4768.
- [42] N. Iguiñiz, R. Frisenda, R. Bratschitsch, A. Castellanos-Gomez, Adv. Mater. 2019, 31, 1807150.
- [43] M. Pena-Alvarez, E. del Corro, A. Morales-Garcia, L. Kavan, M. Kalbac, O. Frank, Nano Lett. 2015, 15, 3139.

www.advancedsciencenews.com

www.small-journal.com

16136829, 0, Downloaded from https://onlinelibrary.wiley.com/doi/10.1002/smll.202310175 by GEORGIA STATE UNIVERSITY, Wiley Online Library on [28/02/2024]. See the Terms

and Condition

) on Wiley Online Library for rules

of use; OA articles are governed by the applicable Creative Commons

- [44] S. Dong, X. Zhang, S. S. P. Nathamgari, A. Krayev, X. Zhang, J. W. Hwang, P. M. Ajayan, H. D. Espinosa, Mater. Today 2022, 52, 31.
- [45] Z. Li, Y. Lv, L. Ren, J. Li, L. Kong, Y. Zeng, Q. Tao, R. Wu, H. Ma, B. Zhao, Nat. Commun. 2020, 11, 1151.
- [46] Z. Liu, M. Amani, S. Najmaei, Q. Xu, X. Zou, W. Zhou, T. Yu, C. Qiu, A. G. Birdwell, F. J. Crowne, Nat. Commun. 2014, 5, 5246.
- [47] H. B. Lee, W.-Y. Jin, M. M. Ovhal, N. Kumar, J.-W. Kang, J. Mater. Chem. C 2019, 7, 1087.
- [48] A. L. S. Eh, A. W. M. Tan, X. Cheng, S. Magdassi, P. S. Lee, Energy Technol. 2018, 6, 33.
- [49] Y. Yoon, K. Ganapathi, S. Salahuddin, Nano Lett. 2011, 11, 3768.
- [50] P. Gant, P. Huang, D. P. de Lara, D. Guo, R. Frisenda, A. Castellanos-Gomez, Mater. Today 2019, 27, 8.

- [51] S. Yu, H. D. Xiong, K. Eshun, H. Yuan, Q. Li, Appl. Surf. Sci. 2015, 325, 27.
- [52] R. Kappera, D. Voiry, S. E. Yalcin, B. Branch, G. Gupta, A. D. Mohite, M. Chhowalla, Nat. Mater. 2014, 13, 1128.
- [53] O. Lopez-Sanchez, D. Lembke, M. Kayci, A. Radenovic, A. Kis, Nat. Nanotechnol. 2013, 8, 497.
- [54] S. Manzeli, A. Allain, A. Ghadimi, A. Kis, Nano Lett. 2015, 15, 5330.
- [55] X. Sang, X. Li, W. Zhao, J. Dong, C. M. Rouleau, D. B. Geohegan, F. Ding, K. Xiao, R. R. Unocic, Nat. Commun. 2018, 9, 2051.
- [56] X. Li, A. A. Puretzky, X. Sang, S. KC, M. Tian, F. Ceballos, M. Mahjouri-Samani, K. Wang, R. R. Unocic, H. Zhao, Adv. Funct. Mater. 2017, 27, 1603850.
- [57] X. Li, M. W. Lin, L. Basile, S. M. Hus, A. A. Puretzky, J. Lee, Y. C. Kuo, L. Y. Chang, K. Wang, J. C. Idrobo, Adv. Mater. 2016, 28, 8240.